Atmos. Meas. Tech., 18, 5705–5715, 2025 https://doi.org/10.5194/amt-18-5705-2025 © Author(s) 2025. This work is distributed under the Creative Commons Attribution 4.0 License.





Developing A Custom-Built Metal Aerosol Processing Chamber: Analysis of Aerosol Coagulation at Low Humidities

Nevil A. Franco, Kyle J. Gorkowski, and Katherine B. Benedict

Earth and Environmental Science Division, Los Alamos National Laboratory, P.O. Box 1663, Los Alamos, NM, US

Correspondence: Kyle J. Gorkowski (gorkowski@lanl.gov) and Katherine B. Benedict (kbenedict@lanl.gov)

Received: 28 March 2025 - Discussion started: 21 May 2025

Revised: 2 September 2025 – Accepted: 3 September 2025 – Published: 22 October 2025

Abstract. We have developed an intermediate size (906 L) aerosol processing chamber, and this work reports on the design and initial characterization of dry aerosol experiments. Specifically, we are determining wall-loss and coagulation correction factors using the observed size distribution measurements for surrogates of common aerosol classes: sodium chloride, sucrose, and biomass burning aerosol smoke. Results show that, on average, sodium chloride, sucrose, and smoke wall-loss rates converge to similar values on relatively short time scales ($<1\,\text{h}$). The fitted coagulation correction factor, W_{C}^{-1} , for smoke particles (1.23 \pm 0.312), indicates that on average they adhere to each other more than sodium chloride (0.969 \pm 0.524) and sucrose (1.16 \pm 1.38). The relative uncertainty is high for the coagulation correction, but it is consistent with our Monte Carlo error analysis.

This study lays the foundation for future experiments at el-

evated humidity and supersaturation conditions to character-

ize the influence of particle shape on coagulation and cloud

1 Introduction

parameters.

Aerosol-cloud interactions remain one of the largest sources of uncertainty in the Earth's radiation budget. By directly scattering, absorbing solar radiation and indirectly influencing cloud formation, aerosols affect longwave and shortwave radiation in the Earth's atmosphere (IPCC, 2023). Despite sustained research efforts, these impacts still pose significant challenges to our understanding of the aerosol cooling effect, estimated at $-0.86\pm0.56\,\mathrm{W\,m^{-2}}$, and the effective anthropogenic radiative forcing of Earth's climate (estimated at $-1.25\pm0.85\,\mathrm{W\,m^{-2}}$) (IPCC, 2023). The complexity of

aerosol sources, properties, and processing continues to hinder precise quantification of these forcing estimates.

A critical source of aerosols is wildfire smoke, which can influence radiative budgets up to a year depending on the transport and evolution of plumes (D'Angelo et al., 2022; Guimond et al., 2023; Yu et al., 2019). Under extreme burning conditions, wildfires can generate pyrocumulonimbus clouds, lofting large concentrations of aerosol into the upper troposphere and lower stratosphere (Leach and Gibson, 2021; Rodriguez et al., 2020; Yu et al., 2019). These smoke particles can exert prolonged effects on climate through chemical and physical processes such as condensation and coagulation (Fromm et al., 2022; Gorkowski et al., 2024; Reisner et al., 2023). The fractal nature of soot particles further complicates our understanding of their indirect effects on cloud formation and radiative properties (Cotton et al., 2011; Das et al., 2021; June et al., 2022). For instance, during the Amazon biomass burning season, Koren et al. (2004) reported a dramatic reduction in cumulus cloud cover – from 38 % under cleaner conditions to 0 % during heavy smoke. However, Kaufman and Koren et al. (2006) observed an increased cloud cover in regions with higher column aerosol concentrations. These discrepancies underscore the complexity of aerosol-cloud interactions, which depend on various factors such as aerosol composition, hygroscopicity, size distribution, supersaturation, and the prevailing atmospheric stability (Feingold et al., 2001). As wildfires increase in frequency and intensity due to climate change (Cunningham et al., 2024), refining our knowledge of how these aerosols evolve and ultimately affect cloud development is crucial for improving climate models and future predictions.

Beyond large-scale aerosol effects, aging aerosols undergo microphysical transformations that can drastically alter their role in cloud processes. Condensation of organics and the mixing of sulfate with black carbon (BC) have both been shown to influence cloud dynamics (Ching et al., 2018). Recent work indicates that larger BC agglomerates may form preferentially at cloud tops, while the thickly-coated BC particles are most likely to be scavenged by cloud droplets (Taylor et al., 2014; Zanatta et al., 2023). Modeling these highly dynamic processes remains challenging, as it requires accurately representing particle growth, mixing states, and cloud interactions (Ching et al., 2016; Riemer et al., 2009; Yang et al., 2023; Yao et al., 2021; Zaveri et al., 2010).

Aerosol chambers are used to understand these chemical and microphysical transformation in controlled conditions (Becker, 2006; Doussin et al., 2023). Many were built for gas-phase and secondary organic aerosol experiments and feature large volumes with Teflon walls to reduce wall losses (Hynes et al., 2005; Shao et al., 2022). Others are optimized for specific aerosol processes, like bioaerosols (Massabò et al., 2018). Cloud chambers are a class of chambers for investigating cloud microphysical mechanisms under wellcontrolled conditions (Chang et al., 2016; Khlystou et al., 1996; Niedermeier et al., 2020; Shao et al., 2022). Existing cloud chambers are their own institutional facility in the case of CLOUD at CERN (The Cloud Collaboration, 2001), AIDA Chamber EUROCHAMP (Wagner et al., 2006), and PI-chamber at MTU (Chang et al., 2016). These types of facilities are critical for advancing science but are often oversubscribed and require significant support to operate.

As outlined in many of the papers cited in the previous paragraph, all chambers however, come with artifacts—most notably, the loss of particles to chamber walls through gravity, diffusion, convection, and electrostatic forces (Corner and Pendlebury, 1951; Fotou and Pratsinis, 1993; Mahfouz and Donahue, 2020a; Wang et al., 2018). Previous studies have highlighted the importance of accounting for both size-dependent and time-dependent wall losses (Crump et al., 1982; Crump and Seinfeld, 1981).

In this paper, we introduce the development of a Los Alamos National Laboratory (LANL) aerosol processing chamber, which we use to investigate coagulation processes under simulated conditions. We present data from experiments where aerosols were injected in a dry environment to quantify losses to chamber walls, dilution, and coagulation effects. Different types of aerosols were examined to validate known aerosol behaviors and characterize coagulation. We further demonstrate the use of a python based aerosol package, Particula (Particula, 2025), to model coagulation and wall-loss rates. Through this study, we aim to characterize the behavior of aerosol in the dry chamber (influence of particle composition and shape) and determine conditions suitable for future studies at elevated humidity including supersaturation. In addition, we perform an uncertainty analysis on the coagulation correction retrieval to determine the range of aerosol concentrations that reduce uncertainty in coagulation corrections.

2 Chamber Development and Methods

2.1 Setup of chamber and experiments

The LANL chamber is in the first phase of development with control of both temperature and humidity to be added in future work. The 906 L (0.906 m³, internal volume) chamber is made of 6 stainless steel walls which are inert and reduce the effects of electrostatic charge. The rectangular body and dimensions are shown in Fig. 1. The chamber has an internal surface area of 6 m² with surface-to-volume ratio of 6.6 m⁻¹. The chamber's joints are sealed with a fast cure marine adhesive caulk (Sika, Sikaflex 291) and the outside junctions where the walls intersect are sealed using ZIP SystemTM Strech Tape (Huber Engineered Woods). Portholes were made for the top and bottom plates where wires and probes be placed for measurements in the chamber and for aerosols to flow in and out of the chamber. Unused portholes are sealed with Swagelok caps and those used for probes and wires are sealed with a rubber gasket or a Teflon ferrule. A leak test was performed by pressurizing the chamber by feeding clean air in and sealing every outlet then seal any leak detected. The chamber is designed to operate at ambient pres-

Copper tubing lines (3/8'') are used to supply aerosols to the chamber and deliver outflow sampling to instrumentation. Zero-air generators (T701 Teledyne Inc., USA) provide clean dry air to push aerosol to the chamber and additional dilution air using Teflon tubing (1/4''). Push flow enters at the bottom of the chamber, creating an upwards direction of flow. Aerosols are sampled from an outlet at the top of the chamber. A dilution flow is connected to the outlet line (88.9 mm from the outlet) to control aerosol concentrations and prevent overwhelming the sampling instruments. A minimum sampling flow rate of 1.5 L min⁻¹ was needed to supply the instruments and we used a 1:5 ratio of push to dilution for the experiments presented here. This infers a residence timescale within the chamber of 604 min (10 h) and half-life of 418 min (6.9 h). The flow rates are controlled with mass flow controllers (MFC; Alicat). Prior to each experiment the chamber was flushed by pushing clean air with a flow of $\sim 10 \, \mathrm{L \, min^{-1}}$ for at least 3 h to reach background (~ 0 –10 cm⁻³).

2.2 Aerosol Generation and Instrumentation

Two aqueous solutions and controlled combustion of dried biomaterial were used as the sources of aerosols. Sodium chloride (NaCl; Sigma-Aldrich) was chosen because it is a well-understood compound in aerosol studies. Sucrose (Sigma-Aldrich) was used to act as a secondary organic aerosol surrogate, and it is also a well-studied aerosol. Each were dissolved in deionized water (Milli-Q, 18.2 $M\Omega$) in separate solutions and were put on an Atomizer Aerosol Generator (3079, TSI Inc., USA). The particles coming out of the atomizer passed through a silica gel diffusion drier

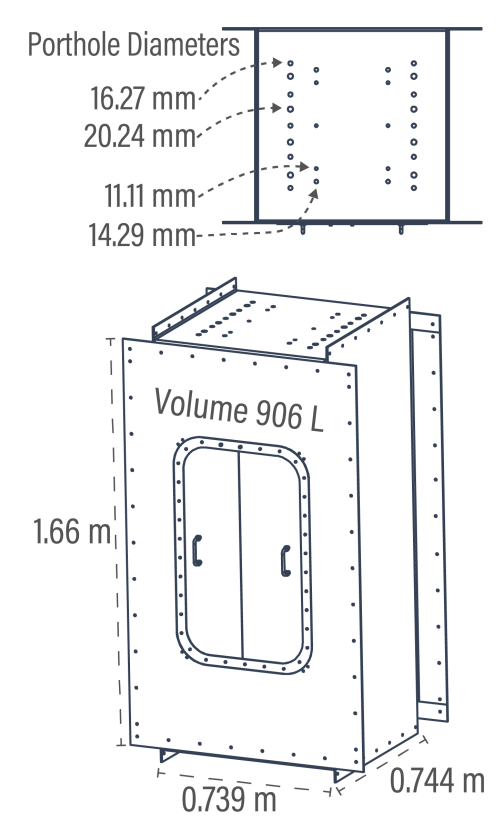


Figure 1. Schematic of LANL's 906 L chamber. The chamber has external dimensions of $1.66\,\mathrm{m}$ in height, $0.739\,\mathrm{m}$ in width, and $0.744\,\mathrm{m}$ in depth. The design includes 56 portholes with diameters ranging from 11.11 to $20.24\,\mathrm{mm}$, shown across the top and mirrored on the bottom.

at a generation flow rate of $\sim 2.4 \, \mathrm{L} \, \mathrm{min}^{-1}$. The duration of aerosol injection varied based on the desired number concentration. To generate smoke, 0.1-0.5 g samples of dried biomaterial Poa pratensis (Kentucky bluegrass) were weighed out, placed on a quartz boat and into a quartz-tube furnace (Carbolite Gero, TS1-1200, Verder Scientific, UK) that was set to 1000 °C for a flaming combustion condition. This identical setup was used in Benedict et al. (2024) which showed that at 1000 °C burn the black carbon mass fraction averaged 17% for biomass fuels with a single scattering albedo of 0.35 (at 523 nm). We expect a similar smoke profile for the experiments presented here thus the smoke injected is a combination of soot, inorganic, and organic mass along with volatile vapors. Smoke particles were pushed to the chamber by zero-air at $4 \,\mathrm{L}\,\mathrm{min}^{-1}$ for $5 \,\mathrm{min}$, a time window used to ensure complete combustion of the sample.

Aerosol size and number distributions downstream of the chamber were measured with a scanning mobility particle sizer (SMPS) that consists of a Differential Mobility Analyzer (3081 DMA, TSI Inc., USA) and a Condensation Particle Counter (3752, TSI Inc., USA). Measurement settings were set to continuously scan for 3 min per scan; 160 s recording with 20 s of purging, measuring sizes 15.7–

764.5 nm. Our experimental matrix consisted of 8 repeats of NaCl, 4 repeats of sucrose and 6 smoke experiments with varying biomaterial mass, they are outlined in Supplement Information Table 1. In all experiments the first 6 h of data were used to analyze results.

3 Theory on Chamber Processes

3.1 Data Analysis Pipeline

The processing of data from the LANL chamber experiments involved two key steps to analyze the underlying aerosol processes of coagulation, wall loss, and dilution (chamber push line). First, we determined the observed size-dependent particle rates: $dN(D_p)/dt$. The measured size distributions were fitted to a two-mode lognormal distribution. The lognormal distribution parameters were optimized using the Python library SciPy's optimization routines, with the mean squared error as the cost function. We used multiple minimization methods and selected the best fit for each timestep based on the highest Pearson R-squared value with a minimum threshold of 0.85. The methods included Nelder-Mead (Simplex algorithm), Powell's method (Powell's conjugate direction method), L-BFGS-B (Limited-memory Broyden-Fletcher-Goldfarb-Shanno with Box constraints), TNC (Truncated Newton Conjugate-Gradient method), SLSQP (Sequential Least Squares Programming), and trust-constr (Trust Region Constrained method). We took this approach since the best fit varied with concentration and shape of the distribution. L-BFGS-B was typically the best for a lognormal distribution, but as the mode became broader (lower concentrations) then TNC, SLSQP or trust-constr would have a higher Pearson Rsquared value. The transition of when this would occur was not an obvious concentration threshold. Therefore, we used all optimization routines for each lognormal distribution and selected the best fit based on the highest Pearson R-squared value.

Second, we fitted these observed rates to theoretical rates calculated from Particula (Particula, 2025), a python-based aerosol microphysics package. The first step was to generate a new time series at a higher size resolution (log-spaced 250 bins), starting at 20 nm and extrapolating the 746 nm SMPS upper limit to 4 µm. The size-dependent particle rate was then computed as the linear slope of 21 point moving window (10 before and 10 after). The time window (60 min) was chosen through iteration, as shorter than 20 min had too much noise to have self-consistent results and longer than 90 min had increasing fit residuals. Our 60 min window results in a smoothed time evolution, which Mahfouz and Donahue (2020a) showed to be effective in coagulation analysis. Our moving window approach is different from smog chamber wall-loss experiments where the full 5 h of the wall-loss experiment would be used to fit an apparent size-dependent, time-invariant wall-loss correction (Wang et al., 2018).

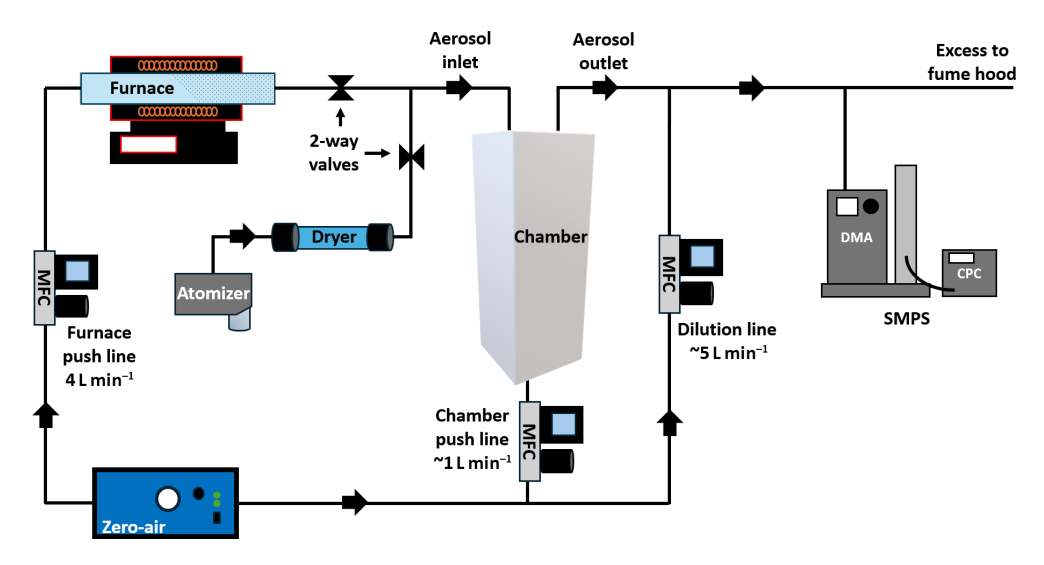


Figure 2. Schematic of experimental setup showing how aerosols are injected and sampled from the chamber.

The resulting size-dependent rate was subsequently used to fit the underlying aerosol processes in Eq. (1) where $N(D_p)$ represents the number concentration of particles of diameter, D_p , K_{12} is the coagulation kernel, W_C^{-1} is the coagulation correction factor, N_1 and N_2 are the concentrations of particles in the bins for K_{12} , k_{flow} is the chamber flow coefficient, and β is the wall-loss rate.

$$\frac{\mathrm{d}N\left(D_{\mathrm{p}}\right)}{\mathrm{d}t} = W_{\mathrm{C}}^{-1} K_{12} N_{1} N_{2} - k_{\mathrm{flow}} N\left(D_{\mathrm{p}}\right) - \beta N\left(D_{\mathrm{p}}\right) \quad (1)$$

The coagulation term is governed by a Brownian Coagulation kernel, K_{12} , that captures the collision frequency between bin number concentrations (N_1 and N_2). This kernel is described in Seinfeld and Pandis (Seinfeld and Pandis, 2016; Sect. 13 – Fuchs form with alpha efficiency 13.56), and calculated with Particula. Since K_{12} does not account for other interactions (e.g. Coulomb interactions) that may lead to coagulation, $W_{\rm C}^{-1}$, the coagulation correction factor, was determined. In our analysis, $W_{\rm C}^{-1}$ is a free fit parameter to allow for un-modeled behaviors to be represented. The chamber flow coefficient, $k_{\rm flow} = Q/V$, characterizes how the clean air flow rate (Q) is used to push sample flow out of the chamber volume (V). Finally, the wall-loss term, $\beta N (D_{\rm p})$, accounts for the size-dependent removal of particles to the chamber walls.

$$\beta = \frac{1}{LWH} \left(\frac{4H (L+W) \sqrt{k_e D}}{\pi} + v_p LW \times \coth\left(\frac{\pi v_p}{4\sqrt{k_e D}}\right) \right)$$
 (2)

Equation (2) shows the wall-loss rate (β) varies with particle size, derived from a rectangular-chamber formulation adapted from Crump and Seinfeld (1981) and Crump et al. (1982). It incorporates both diffusion-driven transport and

gravitational settling. In this formulation, L, W, and H denote the chamber's length, width, and height, respectively; k_e is the eddy wall diffusivity (a free fit parameter); D is the particle diffusion coefficient; and v_p is the particle gravitational settling velocity. This physics-based wall-loss coefficient is different from Wang et al.'s (2018) method of apparent sizedependent wall-loss fit. In the apparent size-dependent wallloss fit the rate equation is a two-term first-order rate equation, where there are no physical terms for the size of the chamber or particle settling velocity, in contrast to what we use in Eq. (2). The apparent size-dependent wall-loss approach is common for smog chamber experiments (Doussin et al., 2023; Keywood et al., 2004; Loza et al., 2012; Nah et al., 2017; Ng et al., 2007) but would not work here since one of our goals is to specifically determine coagulation. In our case, we need a physics-based wall-loss rate equation, so we can determine if there are any coagulation corrections that could be applied. If we had used the apparent size-dependent wall-loss fit, then there would be little to no residuals for a coagulation correction analysis.

3.2 Volume Conservation Analysis

If the corrected aerosol volumes remain consistent, within the noise measurement, we can infer that the processes described in Equation 1 accurately represent chamber behavior. Measured volume concentrations in our experiments were corrected by accounting for volume losses due to both wall loss and chamber flow. We calculated the cumulative lost volume and added it back to the measured values at each time point. In smog chamber experiments involving secondary organic aerosol formation, this volume conservation analysis provides a constraint on organic aerosol yields. Supplemental Fig. S8 shows an example of our volume conservation plot from a smoke injection experiment. From this analysis,

we conclude that volume is conserved and that no measurable condensation of biomass burning organic vapors occurs under our experimental conditions.

4 Results and Discussion

4.1 Example Analysis

We show, in Fig. 3, the L-BFGS-B optimization routine that was used on Eg. (1) for experimental data from the smoke aerosol generated by combusting Kentucky bluegrass. Figure 3a shows the lognormal-fitted size distribution for the entire experiment, where particle growth is evident as the mode diameter shifts to larger sizes over the six-hour period. Figure 3b breaks down the observed rates after 1.5 h into three calculated, time-varying, size-dependent components: coagulation, dilution, and wall-loss. At that time, coagulation dominates, reducing particles around $100 \, \mathrm{nm} \ (\sim 0.16 \, \mathrm{cm}^{-3} \, \mathrm{s}^{-1})$ and forming larger particles around $200 \, \mathrm{nm}$. From these fits we are specifically interested in the kernel correction factor to better understand the importance of agglomeration of freshly emitted BC fractal-like particles and how it changes in time.

4.2 Wall-loss Comparison

In Fig. 4a we show the average wall-loss rates for our three different aerosol types based on 4–8 experiments each. Only results with valid optimizations and an R-squared above 0.85 were included. In the sucrose experiments, this filter led to data gaps during the later time periods (2–6 h) for inclusion in the analysis. To better compare with smoke, we conducted additional NaCl experiments to have a more complete time series for one of the comparisons. The wall-loss rates during the first hour (< 1 h) follow a similar trend apart from NaCl starting at a low wall-loss rate then rising close to a rate of $2 \,\mathrm{s}^{-1}$. These initial wall-loss rates are consistent with the general observation in chamber studies that early mixing processes and injection conditions can dominate particle loss. Typical ranges reported in smog chamber experiments span from $< 1 \,\mathrm{s}^{-1}$ to tens of s^{-1} depending on injection flow and the use of a fan (Zong et al., 2023), particle species (Li et al., 2017; Wang et al., 2011), and chamber geometry (Wang et al., 2011). Over longer times (> 1 h), all three aerosol types converge toward similar wall-loss rates (0.1 s⁻¹), in agreement with the literature indicating that chamber turbulence diminishes over time as mixing subsides.

Figure 4b shows the statistical distribution of the wall-loss rates for each aerosol type during the first hour and the subsequent five hours. NaCl and sucrose do not exhibit a large variance in diffusivity for the first hour compared to smoke which is $1.12\pm1.55\,\mathrm{s^{-1}}$. NaCl, sucrose, and smoke show mean wall-loss rates of $0.562\pm0.975,\,0.233\pm0.286,\,\mathrm{and}\,0.201\pm0.267\,\mathrm{s^{-1}}$, respectively. This convergence to relatively similar values is consistent with past observations in

smog chamber experiments, where turbulent mixing dissipates, and the system approaches a quasi-steady loss rate such as the CMU Teflon chamber (Mahfouz and Donahue, 2020b; Wang et al., 2018), the CESAM chamber (Wang et al., 2011), and the AIR chamber (Zong et al., 2023). However, NaCl and sucrose experiments display greater variability than smoke, likely due to residual chamber turbulence stemming from their distinct generation methods (aerosolization vs. combustion).

4.3 Coagulation Corrections

To investigate the influence of interparticle forces on aerosol coagulation, we fitted a coagulation correction factor that would account for van der Waals forces, shape, and/or Coulomb interactions in the coagulation rate. When $W_{\rm C}^{-1}=1$, collisions are effectively "elastic," with no net enhancement or inhibition. In contrast, $W_{\rm C}^{-1}>1$ indicates that coagulation is enhanced (e.g. due to attractive forces, favorable particle morphology, or turbulence), whereas $W_{\rm C}^{-1}<1$ implies reduced coagulation (e.g. electrostatic repulsion or other inhibiting effects).

In Fig. 5a, the smoke experiments show an initial period where $W_{\rm C}^{-1}>1$, which may be explained by the fractal nature of soot aggregates that can promote sticking or chain formation upon collision. By the third hour in all experiments, accounting for the variation the average coagulation corrections extend above and below 1. During this later phase, particle concentrations ($<10^4 {\rm cm}^{-3}$) no longer sustain significant coagulation losses, consistent with prior studies showing that coagulation becomes negligible under lower concentration conditions (Hussein et al., 2009; Mahfouz and Donahue, 2020b; Yu et al., 2022).

Figure 5b shows the distribution of coagulation corrections for these time periods. All three aerosols show a mean $W_{\rm C}^{-1}$ value around 1 (0.969 \pm 0.524 for NaCl, 1.16 \pm 1.38 for sucrose, and 1.23 \pm 0.312 for smoke), suggesting a slight repulsion or negligible net sticking among particles. However, the standard deviations do encompass $W_{\rm C}^{-1}=1$. Smoke exhibits a slightly higher coagulation corrections initially followed by reduced values (0.941 \pm 0.307) in later periods. These observations align with the notion that both particle morphology (e.g., fractal soot structures) and injection-induced turbulence can transiently enhance coagulation, but the effect diminishes as particles coagulate.

4.4 Monte Carlo Error Analysis

To understand the large standard deviations that emerged from our fits of wall loss and coagulation correction, we performed a Monte Carlo error analysis. We began by constructing three number-size distributions, each formed by the sum of two log-normal modes with equal particle numbers. In the first case both modes were centered at 100 nm but differed in geometric standard deviation (GSD), i.e., the distribution

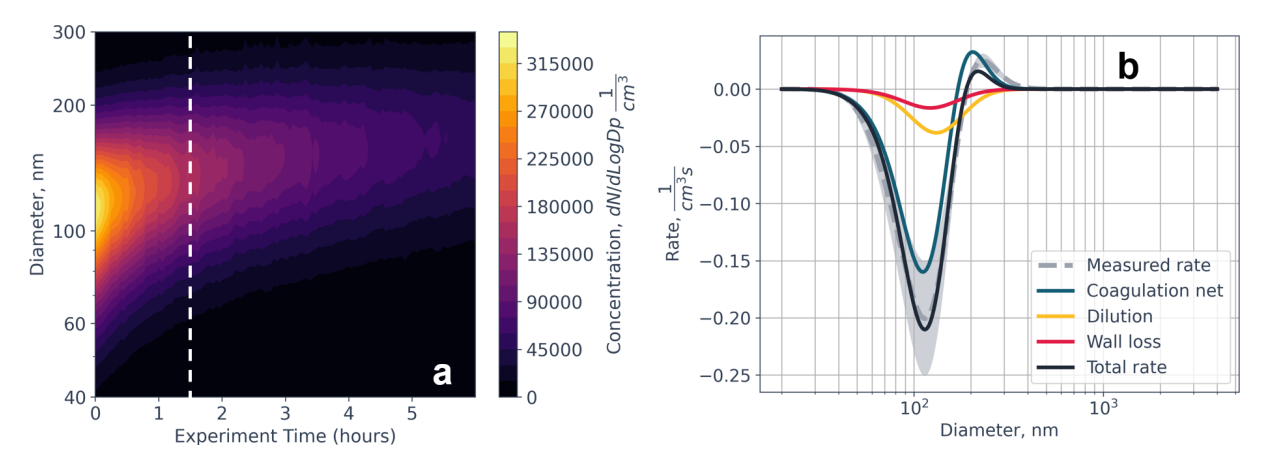


Figure 3. (a) Time series of the lognormal-fitted size distribution and concentration for a smoke experiment. The dashed line marks a time slice at approximately 1.5 h. (b) At this time slice, particle loss rates are calculated, revealing both loss and gain of particles due to coagulation. (The time series of rates for individual aerosol species are provided in the Supplement Figs. S2–4.) In this panel, the dashed gray line represents the measured rate with uncertainty (shaded gray), while the blue, yellow, and pink lines correspond to the coagulation process, dilution, and wall loss, respectively.

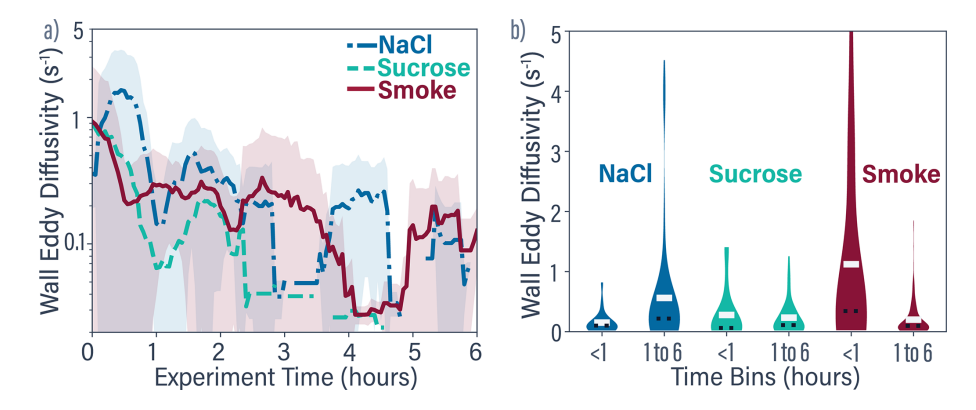


Figure 4. (a) Average time series of the calculated wall eddy diffusivity for NaCl (blue), sucrose (green), and smoke (red). Only fits with valid optimizations and r-squared greater than 0.85 are included. (b) Violin plots showing the mean , median (white bar) and overall distribution range of wall eddy diffusivity values for each aerosol type in two-time bins (< 1 and 1-6 h). The width of each colored region represents the relative density of data points at that value.

is summation of a 100 nm mode with a GSD of 1.4 plus a 100 nm mode with a GSD of 1.8. The resulting distribution reflects the broad distributions we observe in our measurements. The second case repeated this structure at 200 nm. The third case was a hypothetical experiment that combined narrow 100 and 300 nm modes (both GSD = 1.2) to test the response to a bimodal aerosol distribution.

For every distribution we calculated Eq. (1) assuming a wall-eddy diffusivity of $0.1\,\mathrm{s}^{-1}$ and a coagulation correction factor (W_{C}^{-1}) of 1.0. This is a null case in which no additional correction to the Brownian coagulation kernel is required. We then superimposed random noise of $\pm 20\,\%$ on both the size spectrum and the rate. This noise mirrors uncertainties reported in instrument intercomparisons of $\pm 10\,\%$ error between 20 and 200 nm and up to $\pm 30\,\%$ above 200 nm (Wiedensohler et al., 2012). Thus, $\pm 20\,\%$ is a middle point

across the range we measured. Applying the same noise to the rate represents the best-case scenario for our analysis pipeline.

With these noisy data sets created, we refit the wall-eddy diffusivity and coagulation correction 80 times at each total number concentration shown in Fig. 6. From the ensemble of fits we calculated the percent error in each retrieved parameter and averaged the results (Fig. 6). The results in Fig. 6 reveal a clear trend in percent error. When total number concentration exceeds roughly $10^4 \, \mathrm{cm}^{-3}$, the uncertainty in the coagulation correction begins to fall. This is consistent with the fact that Brownian coagulation scales with particle number squared and can be distinguished from measurement noise only at higher concentrations. Conversely, the error in the wall-eddy diffusivity grows with concentration. Once coagulation dominates the particle loss budget, the data con-

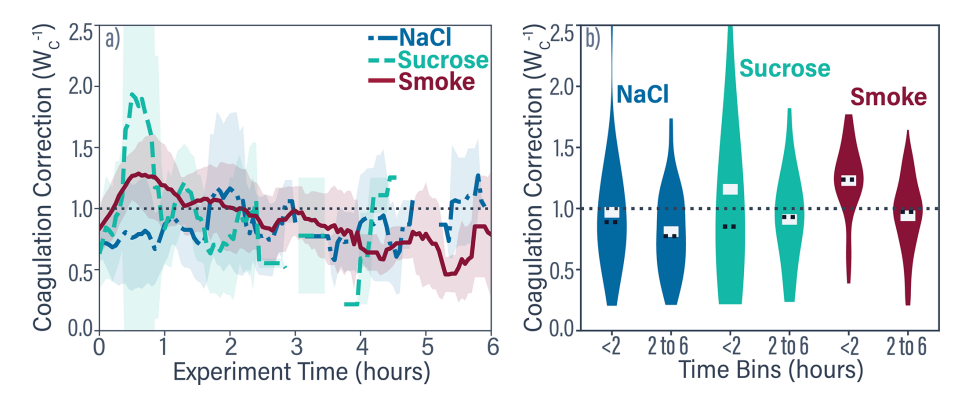


Figure 5. (a) Average time series of the calculated coagulation correction for NaCl (blue), sucrose (green), and smoke (red). Only fits with valid optimizations and r-squared greater than 0.85 are included. (b) Violin plots showing the mean, median (white bar) and range of the calculated coagulation correction for each aerosol type averaged across replicate experiments for the indicated time bins (similar to Fig. 4b).

tains too little information to constrain the comparatively low wall loss sink, increasing the relative uncertainty. In other words, when coagulation governs the system dynamics, the wall-loss term becomes a minor, poorly resolved correction.

The three analyzed distributions exhibit similar percent errors in the coagulation correction. The slightly lower error for the 100 nm mode compared to the 200 nm mode is consistent with the behavior of the Brownian coagulation kernel, where smaller particles have higher coagulation coefficients and therefore undergo more frequent collisions. This leads to a greater rate of change in the distribution for a given number concentration, resulting in better signal-to-noise. The hypothetical bimodal distribution generally shows the lowest uncertainty among the three cases (in our experimental range), although the improvement is modest.

Annotations in Fig. 6 mark the concentration ranges for the three chamber campaigns, sucrose, NaCl, and smoke aerosols. They also indicate the measured coefficient of variation in the mean coagulation correction for each case. The agreement between these annotated uncertainties and the Monte Carlo error analysis confirms that the observed variability is consistent with the measurement noise.

5 Discussion

Our experiments in this new chamber focused on dry conditions and a set of aerosols to quantify how particles evolve in the absence of humidity ($<10\,\%$ relative humidity). Despite the relatively simple setup – no temperature or humidity control – two key insights will be used in future humidified experiments. First, the wall-loss rates converged to similar values across all aerosol types after the first hour, indicating that early differences largely arose from injection flow conditions and subsequent turbulence. Over time, these chamber conditions stabilized, reinforcing the well-documented notion that particle wall losses approach a quasi-steady state as mixing subsides.

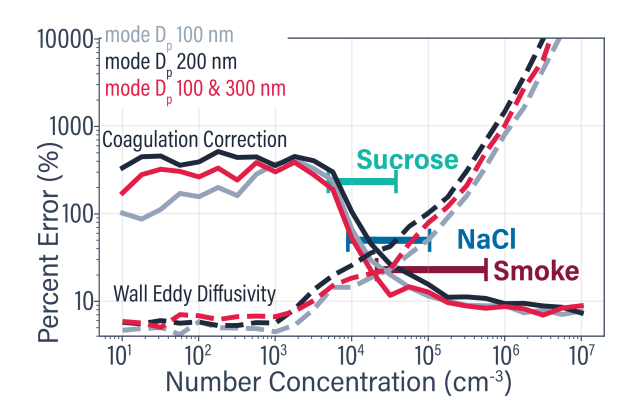


Figure 6. Percent error in fitting of coagulation correction (solid line) and wall eddy diffusivity (dashed line) as a function of number concentration. Lines represent mean errors for size distributions with different modal diameters: 100 nm (gray), 200 nm (black), and a bimodal 100 and 300 nm distribution (red). Annotated markers indicate representative number concentration ranges for Sucrose, NaCl, and Smoke experiments, along with the coefficient of variation (standard deviation divided by the mean) in the coagulation correction, reflecting relative uncertainty rather than bias.

A second important finding is that coagulation within the chamber is most pronounced during the initial phase of each experiment. Though this is more uncertain due to larger relative errors. Smoke showed signs of coagulation enhancement, potentially attributable to its fractal structure. Once total number concentrations fell below a few thousand particles per cubic centimeter, coagulation slowed considerably, consistent with the literature. Collectively, these observations highlight the dynamic interplay between wall loss, particle morphology, and injection protocols in shaping the early stages of aerosol evolution in chamber studies.

Our results also shed light on the influence of particle composition and shape. While aerosols like NaCl and sucrose exhibited expected behavior – average collision enhancements near unity – smoke displayed additional complexity. Early-

time coagulation factors for smoke were moderately elevated, suggesting that soot-fractal aggregates within smoke can have an increased collisional radius. Over longer times, the coagulation rates for all three aerosols converged to near unity or below, indicating negligible net enhancement under steady-state conditions. These observations set the stage for more detailed investigations of fractal-like particles under high humidity environments (> 90 % relative humidity).

Although these initial experiments focused on low humidities, the chamber design allows for temperature and humidity control to be integrated in future work. The Monte Carlo error analysis points to using number concentrations above $10^6 \, \mathrm{cm}^{-3}$ for reducing the percent error in future coagulation correction experiments. Extending to more complex atmospherically relevant aerosol mixtures – such as smoke mixed with organic vapors or inorganic salts – will further elucidate aerosol coagulation interactions. Additionally, the use of more advanced aerosol instrumentation will improve the characterization of particle morphologies and mixing states that evolve during cloud processing.

6 Conclusions

The custom-built 906 L stainless-steel chamber provided reproducible measurements of particle size distributions under dry conditions, confirming its suitability for controlled aerosol research. Although initial turbulence drove high wallloss rates, these converged to stable values across NaCl, sucrose, and smoke. This underscores that injection protocols and mixing strongly influence early aerosol behavior. The chamber's intermediate size and flexible design for future temperature and humidity controls make it a useful platform to investigate aerosol-cloud interactions more comprehensively. Integrating additional measurements of particle shape, chemical composition, and mixing state will further clarify the complexities of aerosol aging and cloud formation. Building on these dry experiments, upcoming work at higher humidity will reveal how aerosol coagulation and phase changes affect cloud processes such as droplet activation and scavenging. By disentangling coagulation, dilution, and wall-loss mechanisms, this chamber ultimately enables rigorous study of aerosol transformations, particularly for smoke, in cloud-relevant environments, helping advance both scientific understanding and climate prediction.

Code and data availability. The python data analysis code is available from corresponding authors.

Supplement. The supplement related to this article is available online at https://doi.org/10.5194/amt-18-5705-2025-supplement.

Author contributions. NAF performed the experiments, contributed to the analysis of the results, and wrote the manuscript. KJG was responsible for the design of the chamber and the study, development of the data analysis methods, and contributed to the writing of the manuscript. KBB contributed to the design of the study, analysis of the results, and contributed to the writing of the manuscript.

Competing interests. The contact author has declared that none of the authors has any competing interests.

Disclaimer. Publisher's note: Copernicus Publications remains neutral with regard to jurisdictional claims made in the text, published maps, institutional affiliations, or any other geographical representation in this paper. While Copernicus Publications makes every effort to include appropriate place names, the final responsibility lies with the authors. Also, please note that this paper has not received English language copy-editing. Views expressed in the text are those of the authors and do not necessarily reflect the views of the publisher.

Acknowledgements. The authors would like to thank Hannah Brink, Ryan Farley, James E. Lee, and Matt Nelson for their feedback on the manuscript. Release Number LA-UR-25-22994.

Financial support. Research presented in this article was supported by the Laboratory Directed Research and Development program of Los Alamos National Laboratory under project number 20230248ER. This work was supported by the U.S. Department of Energy through the Los Alamos National Laboratory. Los Alamos National Laboratory is operated by Triad National Security, LLC, for the National Nuclear Security Administration of U.S. Department of Energy (contract no. 89233218CNA000001).

Review statement. This paper was edited by Zamin A. Kanji and reviewed by three anonymous referees.

References

Particula: Paticula Documentation, https://uncscode.github.io/particula/, last access: 21 July 2025.

Becker, K. H.: Overview on the Development of Chambers for the Study of Atmospheric Chemical Processes, in: Environmental Simulation Chambers: Application to Atmospheric Chemical Processes, Dordrecht, 1–26, https://doi.org/10.1007/1-4020-4232-9_1, 2006.

Benedict, Katherine. B., Lee, J. E., Kumar, N., Badal, P. S., Barbato, M., Dubey, M. K., and Aiken, A. C.: Wildland Urban Interface (WUI) Emissions: Laboratory Measurement of Aerosol and Trace Gas from Combustion of Manufactured Building Materials, ACS EST Air, https://doi.org/10.1021/acsestair.4c00217, 2024.

- Chang, K., Bench, J., Brege, M., Cantrell, W., Chandrakar, K., Ciochetto, D., Mazzoleni, C., Mazzoleni, L. R., Niedermeier, D., and Shaw, R. A.: A Laboratory Facility to Study Gas–Aerosol–Cloud Interactions in a Turbulent Environment: The Π Chamber, Bulletin of the American Meteorological Society, 97, 2343–2358, https://doi.org/10.1175/BAMS-D-15-00203.1, 2016.
- Ching, J., Riemer, N., and West, M.: Black carbon mixing state impacts on cloud microphysical properties: Effects of aerosol plume and environmental conditions, JGR Atmospheres, 121, 5990–6013, https://doi.org/10.1002/2016JD024851, 2016.
- Ching, J., West, M., and Riemer, N.: Quantifying Impacts of Aerosol Mixing State on Nucleation-Scavenging of Black Carbon Aerosol Particles, Atmosphere, 9, 17, https://doi.org/10.3390/atmos9010017, 2018.
- Corner, J. and Pendlebury, E. D.: The Coagulation and Deposition of a Stirred Aerosol, Proc. Phys. Soc. Sect. B, 64, 645–654, https://doi.org/10.1088/0370-1301/64/8/304, 1951.
- Cotton, W. R., Bryan, G., and van den Heever, S. C.: Chapter 5 Radiative transfer in a cloudy atmosphere and its parameterization, in: Storm and Cloud Dynamics, edited by: Cotton, W., Bryan, G., and van den Heever, S., International Geophysics Ser., Academic Press, San Diego, CA, USA, 99, 143–175, https://doi.org/10.1016/S0074-6142(10)09911-0, 2011.
- Crump, J. G. and Seinfeld, J. H.: Turbulent deposition and gravitational sedimentation of an aerosol in a vessel of arbitrary shape, Journal of Aerosol Science, 12, 405–415, https://doi.org/10.1016/0021-8502(81)90036-7, 1981.
- Crump, J. G., Flagan, R. C., and Seinfeld, J. H.: Particle Wall Loss Rates in Vessels, Aerosol Science and Technology, 2, 303–309, https://doi.org/10.1080/02786828308958636, 1982.
- Cunningham, C. X., Williamson, G. J., and Bowman, D. M. J. S.: Increasing frequency and intensity of the most extreme wildfires on Earth, Nat. Ecol. Evol., 8, 1420–1425, https://doi.org/10.1038/s41559-024-02452-2, 2024.
- D'Angelo, G., Guimond, S., Reisner, J., Peterson, D. A., and Dubey, M.: Contrasting Stratospheric Smoke Mass and Lifetime From 2017 Canadian and 2019/2020 Australian Megafires: Global Simulations and Satellite Observations, JGR Atmospheres, 127, e2021JD036249, https://doi.org/10.1029/2021JD036249, 2022.
- Das, S., Colarco, P. R., Oman, L. D., Taha, G., and Torres, O.: The long-term transport and radiative impacts of the 2017 British Columbia pyrocumulonimbus smoke aerosols in the stratosphere, Atmos. Chem. Phys., 21, 12069–12090, https://doi.org/10.5194/acp-21-12069-2021, 2021.
- Doussin, J.-F., Fuchs, H., Kiendler-Scharr, A., Seakins, P., and Wenger, J. (Eds.): A Practical Guide to Atmospheric Simulation Chambers, Springer International Publishing, Cham, https://doi.org/10.1007/978-3-031-22277-1, 2023.
- Feingold, G., Remer, L. A., Ramaprasad, J., and Kaufman, Y. J.: Analysis of smoke impact on clouds in Brazilian biomass burning regions: An extension of Twomey's approach, J. Geophys. Res., 106, 22907–22922, https://doi.org/10.1029/2001JD000732, 2001.
- Fotou, G. P. and Pratsinis, S. E.: A Correlation for Particle Wall Losses by Diffusion in Dilution Chambers, Aerosol Science and Technology, 18, 213–218, https://doi.org/10.1080/02786829308959596, 1993.
- Fromm, M., Servranckx, R., Stocks, B. J., and Peterson, D. A.: Understanding the critical elements of the pyrocumulonimbus storm

- sparked by high-intensity wildland fire, Commun. Earth Environ., 3, 243, https://doi.org/10.1038/s43247-022-00566-8, 2022.
- Gorkowski, K., Koo, E., Jordan, S., Reisner, J., Benedict, K. B., and Dubey, M.: Insights into Pyrocumulus aerosol composition: black carbon content and organic vapor condensation, Environ. Sci.-Atmos., 4, 80–87, https://doi.org/10.1039/D3EA00130J, 2024.
- Guimond, S. R., Reisner, J., and Dubey, M.: The Dynamics of Megafire Smoke Plumes in Climate Models: Why a Converged Solution Matters for Physical Interpretations, J. Adv. Model Earth Syst., 15, e2022MS003432, https://doi.org/10.1029/2022MS003432, 2023.
- Hussein, T., Hruška, A., Dohányosová, P., Džumbová, L., Hemerka, J., Kulmala, M., and Smolík, J.: Deposition rates on smooth surfaces and coagulation of aerosol particles inside a test chamber, Atmospheric Environment, 43, 905–914, https://doi.org/10.1016/j.atmosenv.2008.10.059, 2009.
- Hynes, R. G., Angove, D. E., Saunders, S. M., Haverd, V., and Azzi, M.: Evaluation of two MCM v3.1 alkene mechanisms using indoor environmental chamber data, Atmospheric Environment, 39, 7251–7262, https://doi.org/10.1016/j.atmosenv.2005.09.005, 2005.
- IPCC: Climate Change 2021 The Physical Science Basis: Working Group I Contribution to the Sixth Assessment Report of the Intergovernmental Panel on Climate Change, Cambridge University Press, Cambridge, https://doi.org/10.1017/9781009157896, 2023.
- June, N. A., Hodshire, A. L., Wiggins, E. B., Winstead, E. L., Robinson, C. E., Thornhill, K. L., Sanchez, K. J., Moore, R. H., Pagonis, D., Guo, H., Campuzano-Jost, P., Jimenez, J. L., Coggon, M. M., Dean-Day, J. M., Bui, T. P., Peischl, J., Yokelson, R. J., Alvarado, M. J., Kreidenweis, S. M., Jathar, S. H., and Pierce, J. R.: Aerosol size distribution changes in FIREXAQ biomass burning plumes: the impact of plume concentration on coagulation and OA condensation/evaporation, Atmos. Chem. Phys., 22, 12803–12825, https://doi.org/10.5194/acp-22-12803-2022, 2022.
- Kaufman, Y. J. and Koren, I.: Smoke and Pollution Aerosol Effect on Cloud Cover, Science, 313, 655–658, https://doi.org/10.1126/science.1126232, 2006.
- Keywood, M. D., Varutbangkul, V., Bahreini, R., Flagan, R. C., and Seinfeld, J. H.: Secondary Organic Aerosol Formation from the Ozonolysis of Cycloalkenes and Related Compounds, Environ. Sci. Technol., 38, 4157–4164, https://doi.org/10.1021/es035363o, 2004.
- Khlystou, A., Kos, G. P. A., and Ten Brink, H. M.: A High-Flow Turbulent Cloud Chamber, Aerosol Science and Technology, 24, 59–68, https://doi.org/10.1080/02786829608965352, 1996.
- Koren, I., Kaufman, Y. J., Remer, L. A., and Martins, J. V.: Measurement of the Effect of Amazon Smoke on Inhibition of Cloud Formation, Science, 303, 1342–1345, https://doi.org/10.1126/science.1089424, 2004.
- Leach, R. N. and Gibson, C. V.: Assessing the Potential for Pyroconvection and Wildfire Blow Ups, J. Operational Meteor., 47–61, https://doi.org/10.15191/nwajom.2021.0904, 2021.
- Li, K., Chen, L., Han, K., Lv, B., Bao, K., Wu, X., Gao, X., and Cen, K.: Smog chamber study on aging of combustion soot in isoprene / SO₂ / NO_x system: Changes of mass, size, effective den-

- sity, morphology and mixing state, Atmospheric Research, 184, 139–148, https://doi.org/10.1016/j.atmosres.2016.10.011, 2017.
- Loza, C. L., Chhabra, P. S., Yee, L. D., Craven, J. S., Flagan, R. C., and Seinfeld, J. H.: Chemical aging of *m*-xylene secondary organic aerosol: laboratory chamber study, Atmos. Chem. Phys., 12, 151–167, https://doi.org/10.5194/acp-12-151-2012, 2012.
- Mahfouz, N. G. A. and Donahue, N. M.: Primary ion diffusion charging and particle wall loss in smog chamber experiments, Aerosol Science and Technology, 54, 1058–1069, https://doi.org/10.1080/02786826.2020.1757032, 2020a.
- Mahfouz, N. G. A. and Donahue, N. M.: Primary ion diffusion charging and particle wall loss in smog chamber experiments, Aerosol Science and Technology, 54, 1058–1069, https://doi.org/10.1080/02786826.2020.1757032, 2020b.
- Massabò, D., Danelli, S. G., Brotto, P., Comite, A., Costa, C., Di Cesare, A., Doussin, J. F., Ferraro, F., Formenti, P., Gatta, E., Negretti, L., Oliva, M., Parodi, F., Vezzulli, L., and Prati, P.: ChAMBRe: a new atmospheric simulation chamber for aerosol modelling and bio-aerosol research, Atmospheric Measurement Techniques, 11, 5885–5900, https://doi.org/10.5194/amt-11-5885-2018, 2018.
- Nah, T., McVay, R. C., Pierce, J. R., Seinfeld, J. H., and Ng, N. L.: Constraining uncertainties in particle-wall deposition correction during SOA formation in chamber experiments, Atmos. Chem. Phys., 17, 2297–2310, https://doi.org/10.5194/acp-17-2297-2017, 2017.
- Ng, N. L., Kroll, J. H., Chan, A. W. H., Chhabra, P. S., Flagan, R. C., and Seinfeld, J. H.: Secondary organic aerosol formation from *m*-xylene, toluene, and benzene, Atmos. Chem. Phys., 7, 3909–3922, https://doi.org/10.5194/acp-7-3909-2007, 2007.
- Niedermeier, D., Voigtländer, J., Schmalfuß, S., Busch, D., Schumacher, J., Shaw, R. A., and Stratmann, F.: Characterization and first results from LACIS-T: a moist-air wind tunnel to study aerosol-cloud-turbulence interactions, Atmos. Meas. Tech., 13, 2015–2033, https://doi.org/10.5194/amt-13-2015-2020, 2020.
- Reisner, J. M., Josephson, A. J., Gorkowski, K. J., Koo, E., Thompson, D. K., Schroeder, D., and Dubey, M. K.: Informed Multi-Scale Approach Applied to the British Columbia Fires of Late Summer 2017, JGR Atmospheres, 128, e2022JD037238, https://doi.org/10.1029/2022JD037238, 2023.
- Riemer, N., West, M., Zaveri, R. A., and Easter, R. C.: Simulating the evolution of soot mixing state with a particle-resolved aerosol model, J. Geophys. Res., 114, 2008JD011073, https://doi.org/10.1029/2008JD011073, 2009.
- Rodriguez, B., Lareau, N. P., Kingsmill, D. E., and Clements, C. B.: Extreme Pyroconvective Updrafts During a Megafire, Geophysical Research Letters, 47, e2020GL089001, https://doi.org/10.1029/2020GL089001, 2020.
- Seinfeld, J. H. and Pandis, S. N.: Atmospheric Chemistry and Physics: From Air Pollution to Climate Change, 3rd edn., John Wiley & Sons, Hoboken, NJ, USA, 1152 pp., ISBN 978-1-119-22117-3, 2016.
- Shao, Y., Wang, Y., Du, M., Voliotis, A., Alfarra, M. R., O'Meara, S. P., Turner, S. F., and McFiggans, G.: Characterisation of the Manchester Aerosol Chamber facility, Atmos. Meas. Tech., 15, 539–559, https://doi.org/10.5194/amt-15-539-2022, 2022.
- Taylor, J. W., Allan, J. D., Allen, G., Coe, H., Williams, P. I., Flynn, M. J., Le Breton, M., Muller, J. B. A., Percival, C. J., Oram, D., Forster, G., Lee, J. D., Rickard, A. R., Parrington,

- M., and Palmer, P. I.: Size-dependent wet removal of black carbon in Canadian biomass burning plumes, Atmos. Chem. Phys., 14, 13755–13771, https://doi.org/10.5194/acp-14-13755-2014, 2014.
- The Cloud Collaboration: A study of the link between cosmic rays and clouds with a cloud chamber at the CERN PS, https://doi.org/10.48550/ARXIV.PHYSICS/0104048, 2001.
- Wagner, R., Bunz, H., Linke, C., Möhler, O., Naumann, K.-H., Saathoff, H., Schnaiter, M., and Schurath, U.: Chamber Simulations of Cloud Chemistry: The AIDA Chamber, in: Environmental Simulation Chambers: Application to Atmospheric Chemical Processes, Vol. 62, edited by: Barnes, I. and Rudzinski, K. J., Kluwer Academic Publishers, Dordrecht, 67–82, https://doi.org/10.1007/1-4020-4232-9_5, 2006.
- Wang, J., Doussin, J. F., Perrier, S., Perraudin, E., Katrib, Y., Pangui, E., and Picquet-Varrault, B.: Design of a new multi-phase experimental simulation chamber for atmospheric photosmog, aerosol and cloud chemistry research, Atmos. Meas. Tech., 4, 2465–2494, https://doi.org/10.5194/amt-4-2465-2011, 2011.
- Wang, N., Jorga, S. D., Pierce, J. R., Donahue, N. M., and Pandis, S. N.: Particle wall-loss correction methods in smog chamber experiments, Atmos. Meas. Tech., 11, 6577–6588, https://doi.org/10.5194/amt-11-6577-2018, 2018.
- Wiedensohler, A., Birmili, W., Nowak, A., Sonntag, A., Weinhold, K., Merkel, M., Wehner, B., Tuch, T., Pfeifer, S., Fiebig, M., Fjäraa, A. M., Asmi, E., Sellegri, K., Depuy, R., Venzac, H., Villani, P., Laj, P., Aalto, P., Ogren, J. A., Swietlicki, E., Williams, P., Roldin, P., Quincey, P., Hüglin, C., Fierz-Schmidhauser, R., Gysel, M., Weingartner, E., Riccobono, F., Santos, S., Grüning, C., Faloon, K., Beddows, D., Harrison, R., Monahan, C., Jennings, S. G., O'Dowd, C. D., Marinoni, A., Horn, H.-G., Keck, L., Jiang, J., Scheckman, J., McMurry, P. H., Deng, Z., Zhao, C. S., Moerman, M., Henzing, B., de Leeuw, G., Löschau, G., and Bastian, S.: Mobility particle size spectrometers: harmonization of technical standards and data structure to facilitate high quality long-term observations of atmospheric particle number size distributions, Atmos. Meas. Tech., 5, 657–685, https://doi.org/10.5194/amt-5-657-2012, 2012.
- Yang, F., Hoffmann, F., Shaw, R. A., Ovchinnikov, M., and Vogelmann, A. M.: An Intercomparison of Large-Eddy Simulations of a Convection Cloud Chamber Using Haze-Capable Bin and Lagrangian Cloud Microphysics Schemes, J. Adv. Model Earth Syst., 15, e2022MS003270, https://doi.org/10.1029/2022MS003270, 2023.
- Yao, Y., Dawson, M. L., Dabdub, D., and Riemer, N.: Evaluating the Impacts of Cloud Processing on Resuspended Aerosol Particles After Cloud Evaporation Using a Particle-Resolved Model, JGR Atmospheres, 126, e2021JD034992, https://doi.org/10.1029/2021JD034992, 2021.
- Yu, H., Gu, H., Sun, Z., Zhou, Y., Chen, J., and Li, Y.: Experimental and Numerical Study on the Gravitational Deposition and Coagulation of Aerosols, Front. Energy Res., 10, 840503, https://doi.org/10.3389/fenrg.2022.840503, 2022.
- Yu, P., Toon, O. B., Bardeen, C. G., Zhu, Y., Rosenlof, K. H., Portmann, R. W., Thornberry, T. D., Gao, R.-S., Davis, S. M., Wolf, E. T., De Gouw, J., Peterson, D. A., Fromm, M. D., and Robock, A.: Black carbon lofts wildfire smoke high into the stratosphere to form a persistent plume, Science, 365, 587–590, https://doi.org/10.1126/science.aax1748, 2019.

- Zanatta, M., Mertes, S., Jourdan, O., Dupuy, R., Järvinen, E., Schnaiter, M., Eppers, O., Schneider, J., Jurányi, Z., and Herber, A.: Airborne investigation of black carbon interaction with low-level, persistent, mixed-phase clouds in the Arctic summer, Atmos. Chem. Phys., 23, 7955–7973, https://doi.org/10.5194/acp-23-7955-2023, 2023.
- Zaveri, R. A., Barnard, J. C., Easter, R. C., Riemer, N., and West, M.: Particle-resolved simulation of aerosol size, composition, mixing state, and the associated optical and cloud condensation nuclei activation properties in an evolving urban plume, J. Geophys. Res., 115, 2009JD013616, https://doi.org/10.1029/2009JD013616, 2010.
- Zong, T., Wu, Z., Wang, J., Bi, K., Fang, W., Yang, Y., Yu, X., Bao, Z., Meng, X., Zhang, Y., Guo, S., Chen, Y., Liu, C., Zhang, Y., Li, S.-M., and Hu, M.: A new smog chamber system for atmospheric multiphase chemistry study: design and characterization, Atmos. Meas. Tech., 16, 3679–3692, https://doi.org/10.5194/amt-16-3679-2023, 2023.